Astroparticle Physics 82 (2016) 36–48

Contents lists available at ScienceDirect

Astroparticle Physics

journal homepage: www.elsevier.com/locate/astropartphys

Simulating the optical performance of a small-sized telescope with secondary optics for the Cherenkov Telescope Array

Cameron Rulten[a,1,*], Andreas Zech[b], Akira Okumura[c,d,e], Philippe Laporte[f], Jürgen Schmoll[g]

[a] School of Physics and Astronomy, University of Minnesota, 116 Church Street SE, Minneapolis, MN 55455, USA
[b] LUTH, Observatoire de Paris, CNRS, Université Paris Diderot, 5 Jules Janssen, Meudon, France
[c] Department of Physics and Astronomy, University of Leicester, University Road, Leicester LE1 7RH, UK
[d] Institute for Space-Earth Environmental Research, Nagoya University, Furo-cho, Chikusa-ku, Nagoya, Aichi 464-8601, Japan
[e] Max-Planck-Institut für Kernphysik, P.O. Box 103980, Heidelberg D69029, Germany
[f] GEPI, Observatoire de Paris, CNRS, Université Paris Diderot, 5 Jules Janssen, Meudon, France
[g] University of Durham, Department of Physics, Durham DH1 3LE, UK

ARTICLE INFO

Article history:
Received 11 January 2016
Revised 26 April 2016
Accepted 11 May 2016
Available online 18 May 2016

Keywords:
Cherenkov Telescope Array
CTA
Gamma-ray astronomy
Schwarzschild–Couder
IACT

ABSTRACT

The Gamma-ray Cherenkov Telescope (GCT) is a small-sized telescope (SST) that represents one of three novel designs that are based on Schwarzschild–Couder optics and are proposed for use within the Cherenkov Telescope Array (CTA). The GAmma-ray Telescope Elements (GATE) program has led an effort to build a prototype of the GCT at the Paris Observatory in Meudon, France. The mechanical structure of the prototype, known as the SST-GATE prototype telescope, is now complete along with the successful installation of the camera. We present the results of extensive simulation work to determine the optical performance of the SST-GATE prototype telescope. Using the *ROBAST* software and assuming an ideal optical system, we find the radius of the encircled point spread function (θ_{80}) of the SST-GATE to be ~1.3 arcmin (~0.02°) for an on-axis ($\theta_{\text{field}} = 0^{\circ}$) observation and ~3.6 arcmin (~0.06°) for an observation at the edge of the field of view ($\theta_{\text{field}} = 4.4^{\circ}$). In addition, this research highlights the shadowing that results from the stopping of light rays by various telescope components such as the support masts and trusses. It is shown that for on-axis observations the effective collection area decreases by approximately 1 m^2 as a result of shadowing components other than the secondary mirror. This is a similar loss (~11%) to that seen with the current generation of conventional Davies–Cotton (DC) Cherenkov telescopes. An extensive random tolerance analysis was also performed and it was found that certain parameters, especially the secondary mirror z-position and the tip and tilt rotations of the mirrors, are critical in order to contain θ_{80} within the pixel limit radius for all field angles. In addition, we have studied the impact upon the optical performance of introducing a hole in the center of the secondary mirror for use with pointing and alignment instruments. We find that a small circular area (radius < 150 mm) at the center of the secondary mirror can be used for instrumentation without any significant impact upon optical performance. Finally, we studied the impact of reducing the size of the primary mirror for the prototype telescope and found that this comes at the cost of poorer image quality and light collection efficiency for all field angles, but at a significant cost saving for a one-off prototype.

1. Introduction

The Cherenkov Telescope Array (CTA) [1] will be the world's first ground-based gamma-ray observatory open to the wider astrophysics community. To achieve an order of magnitude greater sensitivity compared to existing ground-based experiments, the baseline design of CTA will be comprised of telescopes of 3 different sizes; large-sized telescopes (LSTs; diameter ~23 m), medium-sized telescopes (MSTs; diameter ~12 m) and small-sized telescopes (SSTs; diameter ~4 m). To achieve full sky coverage, CTA will consist of two sites, one in the northern and one in the southern hemisphere. One possible layout (shown in previous Monte Carlo studies [2]) for the southern site includes 4 LSTs, 23 MSTs and about 70 SSTs, while the northern array will be smaller, with a possible layout including 4 LSTs, 17 MSTs and probably no SSTs. The SST will be optimized for observing Cherenkov light tracing gamma-rays with energies above a few teraelectron volts (TeV). At

* Corresponding author. Tel.: +1 612-624-7375.
E-mail address: rulten@physics.umn.edu (C. Rulten).
[1] Previously at LUTH, Observatoire de Paris, CNRS Université Paris Diderot, 5 Jules Janssen, Meudon, France.

http://dx.doi.org/10.1016/j.astropartphys.2016.05.002

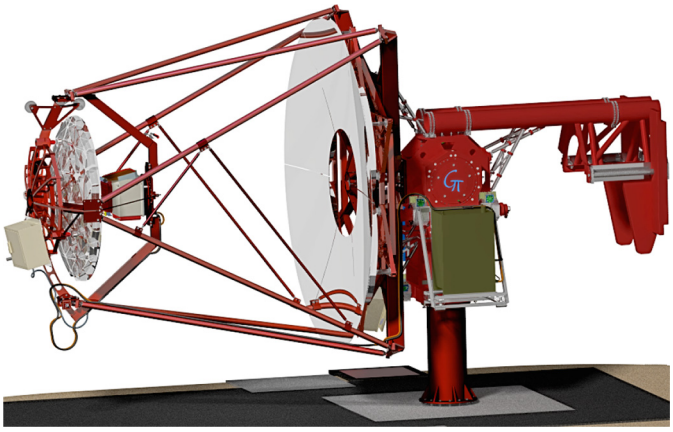

Fig. 1. Computational illustration of the GCT telescope proposed for CTA. The GCT telescope consists of telescope and camera subprojects: SST-GATE and CHEC. The prototype has been built at the Meudon site of the Observatoire de Paris in France. Image credit: GEPI, Observatoire de Paris.

such very high energies, gamma-rays interact with the atmosphere to trigger electromagnetic cascades ("air showers"), which emit a flash (duration of a few ns) of Cherenkov light in the direction close to the shower axis. This emission can be detected in the optical, near-infrared and ultra-violet range and is analyzed to reconstruct the arrival direction and energy of the primary gamma-rays.

CTA is currently investigating three SST designs [3], each of which aims to combine a wide field of view (FOV) with a very good imaging resolution, all the while attempting to keep costs down in order to build ~70 SSTs spread over a few km^2. One of the designs employs a traditional 4 m Davies–Cotton optical system [4] [5], while the other two employ Schwarzschild–Couder (SC) [6] [7] [8] configurations that comprise aspherical primary and secondary mirrors (see Fig. 1). In parallel, other research groups involved in CTA are pursuing an additional telescope type in the form of a 9 m SC telescope system [9]. The SC-based telescope systems proposed for CTA make use of a secondary mirror to reduce the plate scale and to allow for a wide FOV with a light-weight camera.

One of the SC-based SST designs proposed for CTA is called the Gamma-ray Cherenkov Telescope (GCT). The GAmma-ray Telescope Elements (GATE) program has led an effort to build a prototype of the GCT at the Paris Observatory in Meudon, France. The mechanical structure of the prototype is known as the SST-GATE prototype telescope. Thus the GCT is one of the SC configuration projects, which consists of telescope and camera subprojects: SST-GATE and Compact High Energy Camera (CHEC) [10] [11]. There are two prototype versions of CHEC: CHEC-M will use Multi-Anode Photo Multiplier Tubes (MAPMTs) and CHEC-S will use Silicon-based Photo Multipliers (SiPMs).

One of CTA's key motivations for considering the use of dual-mirror SSTs is in the potential to reduce cost, which typically for a Davies–Cotton configuration is dominated by the camera construction, while taking advantage of new high-performance detector technologies. This is achieved through an optimized optical design combining a large FOV with very small aberration effects and a very compact plate scale. Compared to DC telescopes, calculating the tolerances (and hence optical performance) for an SC-optics telescope can be difficult due to the secondary mirror, aspherical surfaces and the very small spot size. This paper highlights the results of detailed simulations conducted to assess the optical performance of the SST-GATE prototype telescope, and for the first time, attempts to show comprehensive tolerance analysis of an SC Cherenkov telescope.

Table 1
SST-GATE specifications.

Primary mirror diameter	4 m
Secondary mirror diameter	2 m
Effective collection area	~ 8.2 m^2
Field of view	9°
Plate scale	39.6 mm/°
Total mass	8 t

Section 2 of this paper will provide a brief outline of the SST-GATE telescope and optical system. Section 3 will highlight simulations of the ideal SST-GATE optical performance. This will include discussion of the point spread function (θ_{80}), effective collection area and telescope shadowing. Section 4 will show the results of a comprehensive tolerance analysis conducted for the SST-GATE telescope. Section 5 will highlight the results of a study undertaken to determine the feasibility of using a small area at the center of the secondary mirror for calibration equipment. Finally, Section 6 illustrates the impact on the optical performance expected as a result of trimming the primary mirror petals of the SST-GATE prototype telescope.

2. The SST-GATE telescope and optical system

The mechanical structure of the SST-GATE prototype telescope [12] [13] has been built at the Meudon site of the Paris Observatory in France [14]. Installation of 2 (out of 6) primary mirror petals (polished aluminum), the secondary mirror (polished aluminum), along with the CHEC-M camera is complete and the prototype telescope was inaugurated on the 1st December 2015. Table 1 highlights the specifications of the telescope, which includes two mirror surfaces that can be characterized by 16th order polynomials. These aspherical mirror surfaces allow for an optimal θ_{80} over the whole 9 degree field of view. The primary mirror is comprised of 6 individual petals while the secondary is a formed monolithic mirror. The original SST-GATE optical design concepts and tolerance analyses were conducted by Jürgen Schmoll and colleagues at Durham University. Since 2011 the project has been led by the SST-GATE group and in particular by teams at the Observatoire de Paris.

The introduction of a secondary mirror leads to ~25% of light rays being obscured. The shadowing that results from the secondary means that a hole of 65 cm radius at the center of the primary mirror can be used for a laser-based alignment system. Each primary mirror segment is attached to the telescope's mechanical structure by three actuators allowing the position of each petal to be adjusted in order to achieve the best possible optical alignment. The secondary mirror will be monolithic and will also be attached to the mechanical structure using actuators to facilitate its alignment.

The SST-GATE ideal focal plane is ~36 cm in diameter and has a 1 m radius of curvature. It is located between the primary and secondary mirror. The ideal focal plane is used for all calculations in this work; however the actual focal plane will be comprised of either MAPMTs or SiPMs. These will be positioned to match the focal plane curvature, but the detector front-end is likely to have a certain fraction of dead space (~3 mm) between each module. In the case of the MAPMT modules this space will be smaller than a single pixel of 6 mm × 6 mm. The optical spot generated on the focal plane for an on-axis observation is expected to be of 4 mm diameter in terms of 80 percent encircled energy. The approximation of the curved focal plane by tiles (e.g. using MAPMT modules) introduces insignificant image spot shape changes, thus the results shown herein (produced using an ideal focal plane) should not be significantly different.

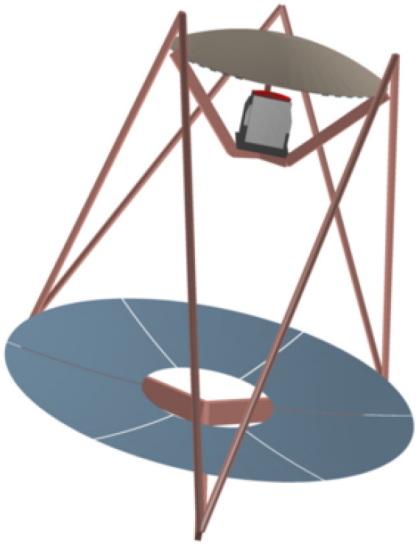

Fig. 2. Computational model of the SST-GATE telescope `2014 design`. This model is used for the tolerance analysis results in Section 4. The structural strengthening implemented in the `final design` does not result in a significant change to the derived PSF. Thus an updated tolerance analysis using the `final design` computational model is not expected to differ from the tolerance analysis results shown in this paper.

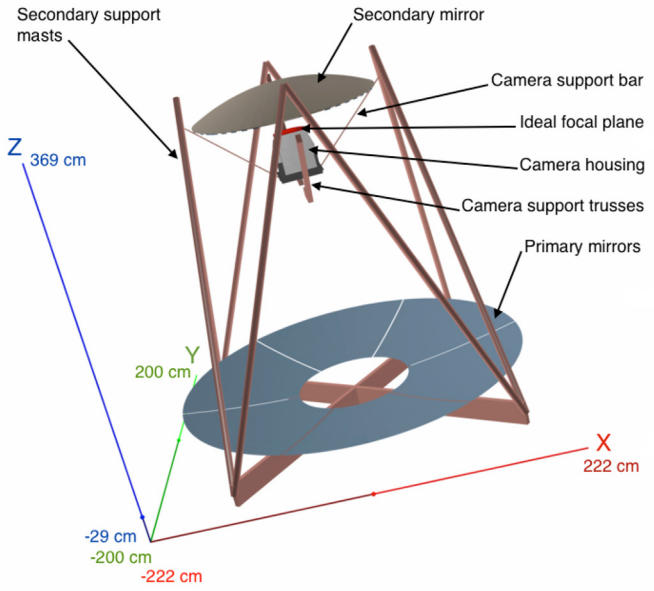

Fig. 3. Computational model of the SST-GATE telescope `final design` proposed for CTA. Shown here are the telescope's 2 optical surfaces: a primary mirror comprised of 6 petals and a monolithic secondary mirror. In addition, the secondary mirror support masts are shown along with the camera support trusses and the camera housing which includes an ideal focal plane (red) on top. This computational model is used for the simulation results highlighted in Sections 3, 5 and 6. (For interpretation of the references to color in this figure legend, the reader is referred to the web version of this article.)

The telescope design has been optimized to keep the maximum incidence angle of photons hitting the curved focal plane below 60° with respect to the normal of the plane. At 60° the visible pixel area for an incoming beam is halved as it scales with the cosine of the angle of incidence. In addition, there is the chance that detector surfaces become less efficient at larger angles due to Fresnel losses. Restricting the marginal angles to 60° ensures that these effects are kept under some control to reduce losses at the detector plane. In fact the final model does not exceed the constraint significantly, with the largest marginal beam incidence at the field edge being 61°.

The mechanical structure of the SST-GATE telescope [15] is made of steel. The main mechanical components include a tower with fork mount and the azimuth and elevation drives, which are based on electric torque motors. The rest of the mechanical system is based on a mast and truss structure, again made from steel, and using a Serrurier [16] configuration which mounts the secondary support structure and camera support structure on the telescope. The preliminary SST-GATE design (now referred to as the `2014 design`) had three camera support trusses, fixing the camera to the support of the secondary mirror, and three pairs of masts that connect the secondary mirror to the main frame. Fig. 2 shows a computational model of the `2014 design`. Following improved Finite Element Analysis (FEA), the SST-GATE telescope `2014 design` evolved as changes were made to reinforce the structure. The prototype telescope constructed at the Observatoire de Paris follows this updated design (now referred to as the `final design`) which includes a fourth pair of secondary support masts (see Fig. 3). Furthermore all the secondary support masts have a smaller diameter compared to those of the `2014 design`. In addition, the number of camera support trusses has been reduced to 2 and a pair of thin camera support bars (12 mm diameter) has been introduced.

Finally, the telescope uses an adaptable counter-weight to balance the loads and the overall telescope mass is expected to be approximately 8 tonnes, making the SST-GATE telescope a relatively light-weight Cherenkov telescope.

3. Simulations of the ideal optical performance

The detailed studies of the SST-GATE optical performance discussed here were carried out principally with the *ROOT* [17] based *ROBAST* [18] ray tracing software. The commercially available *Zemax* [19] ray tracing software was also used for some studies and cross-checks were also made with the *sim_telarray* software [20], which is also used for the published performance simulations of CTA. Details of the ray-tracing software used are limited to *ROBAST*, but for the results herein we indicate (if appropriate) which package was used.

A three dimensional (3D) computer model of the core SST-GATE optical components was constructed using the *ROOT* geometry library and additional *ROBAST* classes. Fig. 3 illustrates the computational model of the `final design` SST-GATE telescope used for the *ROBAST* ray tracing simulations in Sections 3, 5 and 6. Fig. 2 shows the *ROBAST* computational model of the `2014 design` used for the tolerance analysis conducted in Section 4.

Non-sequential ray tracing was performed in *ROBAST* using two methods: parallel rays and rays randomly distributed within a cone from a point at a given distance. The ray tracing of parallel rays was done using a square grid configuration with a single side length of $2.2 \times R_{\text{primary}}$ where R_{primary} is the radius of the primary mirror. In total $\sim 1.6 \times 10^5$ rays were distributed equally over this square grid structure and the parallel rays were traced from a height of ~8 m above the telescope. For the second method the rays were traced from a point situated at 10 km above the telescope, a similar height to that where Cherenkov light is produced in air showers induced by astrophysical gamma-rays. The cone used to confine the paths of the randomly generated rays had a ground radius of $1.1 \times R_{\text{primary}}$. In total $\sim 1.5 \times 10^5$ rays were randomly distributed within this cone. Both methods lead to consistent results for sources close to infinity. For this work the random

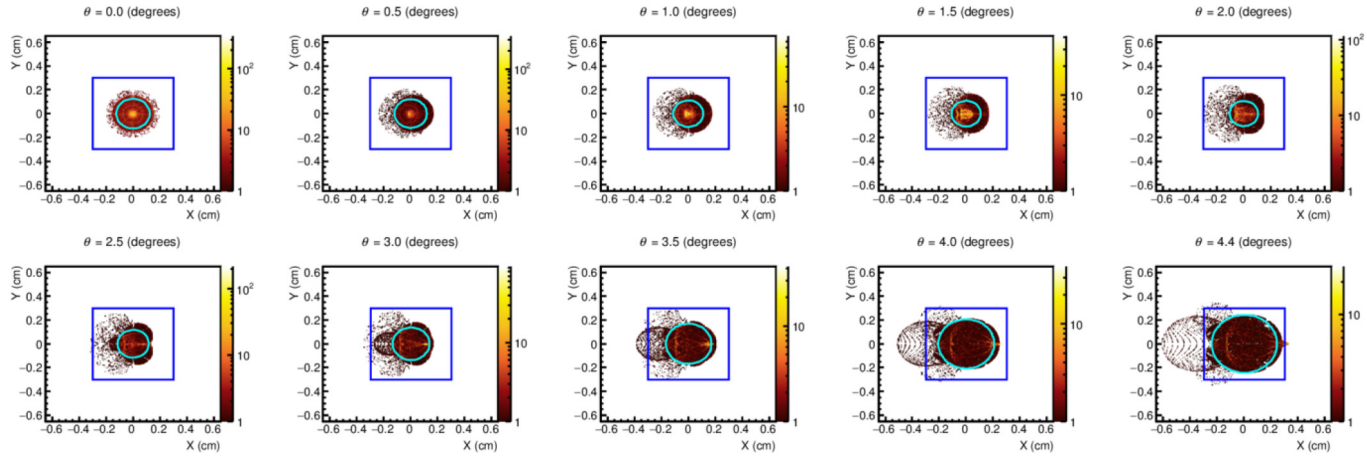

Fig. 4. Shown here are the spots generated on the ideal focal plane of the SST-GATE telescope. Each panel is a 1.3 cm × 1.3 cm area on the focal plane centered on the spot center of mass generated for a given field angle (θ). The color scale illustrates the photon number and the box (solid blue line) illustrates the expected camera pixel size (6 mm × 6 mm). The circle (solid cyan line) shows the derived encircled θ_{80} (see Section 3.1) which is defined as the radius within which 80% of the photons lie. The aberrations seen off-axis give rise to a larger core of the point spread function and an outward pointing coma tail. In the above sequence of images, the spot is moving over the focal plane from left to right with increasing field angle, i.e. the center of the camera is to the left for angles > 0°. (For interpretation of the references to color in this figure legend, the reader is referred to the web version of this article.)

cone ray-tracing method is used for all the quoted values unless otherwise specified.

For the purposes of determining the optical performance parameters an ideal focal plane is used. Photons focused at the ideal focal plane, shown in Fig. 4, are then used to calculate the various performance parameters.

3.1. Point spread function and imaging performance

Within CTA, the imaging performance of a telescope is characterized with θ_{80} and this is defined as the radius that contains 80} of the photons which form the optical point spread function. For this work, θ_{80} was calculated by firstly determining the spot center of mass (COM) which is defined as the arithmetic mean of the photon distributions along both the focal plane x-axis and y-axis. Beginning with an arbitrarily-sized circle centered on the spot image COM, the fraction of photons contained within the circle was calculated. The circle radius was increased in steps of 0.001 cm until the fraction of photons contained within the circle was equal to or greater than the required 80%. This encircled method was conducted for each of the field angles tested, as shown by the red circles in Fig. 4. At a field angle $\theta_{\text{field}} = 4.5^\circ$ the light spot hits the physical limit of the focal plane, within the SST-GATE computational model constructed for this work. This analysis is limited to a field angle of $\theta_{\text{field}} = 4.4^\circ$ which approximately corresponds to the center-point of a pixel if it were placed flush to the edge of the 9 degree field of view.

In addition to the encircled method described above, we also derived θ_{80} using an ensquared method. The process was similar to the encircled method except that 80% of the photons need to be contained within a square, the half−length of which defined the θ_{80} value. Starting at the spot image COM an arbitrary square was defined. The square half−length was increased in steps of 0.001 cm until the fraction of photons contained within the square was equal to or greater than the required 80%. From an error budget point of view, determining θ_{80} using the ensquared method is preferable as the imaging pixels are also square. From a performance budget point of view, the tolerance analysis results highlighted in Section 4 provides the system engineers with the technical margins for which the optical performance remains within specifications. For example, a $\theta_{80} = 2$ mm for an ideal optical performance restricts any increase in the spot radius due to misalignments of the mirrors or camera or other effects to 1 mm, above which the spot ceases to be fully contained inside a pixel.

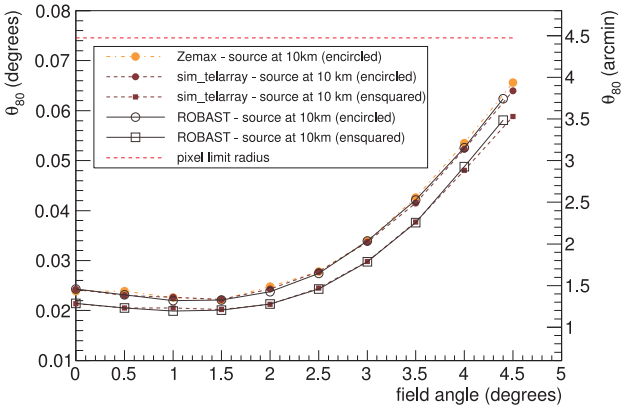

Fig. 5. Shown here are the independently simulated θ_{80} values derived as a function of field angle for the SST-GATE telescope. All of the θ_{80} values were calculated for a point source at a distance of 10 km. The *sim_telarray* (maroon dashed line filled circles), *ROBAST* (black solid line open circles) and *Zemax* (yellow dash dot line filled circles) derived θ_{80} values were calculated using the encircled method. The *sim_telarray* (maroon dashed line filled squares) and the *ROBAST* (black dashed line open squares) derived θ_{80} values were calculated using the ensquared method. Both of the *ROBAST* derived θ_{80} values include additional (to the secondary mirror) shadowing effects due to the presence of the secondary mirror support masts, the camera support trusses and the camera housing. The left axis shows θ_{80} in units of degrees and the right in units of arc minutes. The stepping radius (or half-length) has been plotted as the error bar for each point on this plot, but they are too small to be visible. (For interpretation of the references to color in this figure legend, the reader is referred to the web version of this article.)

The SST-GATE θ_{80} value derived using *ROBAST* was compared against θ_{80} values calculated using different software packages. As previously mentioned, ray-tracing analysis for the SST-GATE was also conducted using the commercially available ray-tracing software *Zemax*. In addition, we also used the Monte Carlo simulation software used in CTA *sim_telarray*. The evolution of θ_{80} as a function of field angle for these independently derived SST-GATE θ_{80} values is shown in Fig. 5. All of the θ_{80} values were calculated for a point source at a distance of 10 km using either the encircled

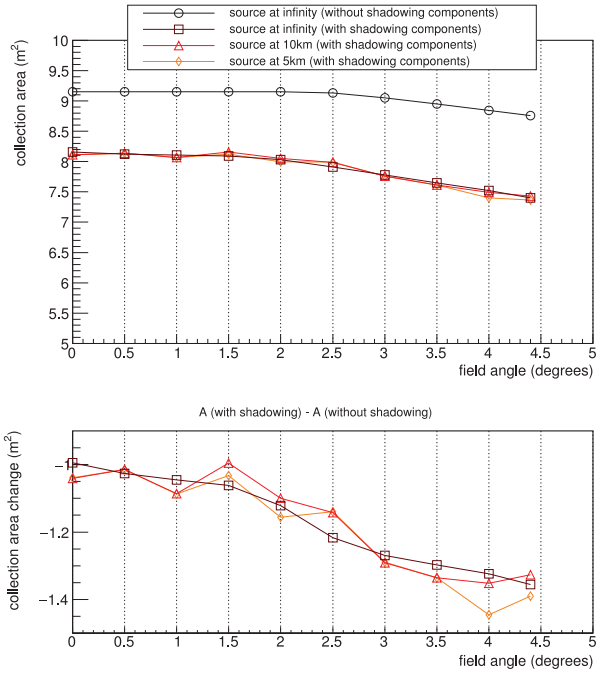

Fig. 6. The top panel shows the effective collection area (for a single rotation angle) as a function of field angle for a single SST-GATE telescope. The effective collection area was calculated for a light source at three different distances: infinity (black line with open circles and maroon line with open squares), 10 km (red line with open upward triangles) and 5 km (yellow line with open diamonds). Shadowing of the secondary mirror is taken into account for all curves. Using the effective collection areas shown in the top panel, the bottom panel shows the difference between the effective collection areas that include shadowing components and the effective collection area without shadowing components. The colors and symbols for each of these correspond with the top panel. (For interpretation of the references to color in this figure legend, the reader is referred to the web version of this article.)

(filled circles) or ensquared (open squares) method. It can be seen that the ideal θ_{80} value is about a factor of three smaller than the pixel size (6 mm) for most of the FOV and remains below the pixel limit up to its edge. As expected the ensquared method returns a better θ_{80} performance, owing to the different definitions in both methods. In conclusion, all the derived θ_{80} values are in very good agreement with one another.

3.2. Effective collection area and shadowing analysis

The effective collection area for the SST-GATE telescope was calculated using $A_{\text{effective}} = \frac{N_{\text{focused}}}{N_{\text{simulated}}} \times A_{\text{simulation}}$ where N is the number of photons and A the area. Therefore, this definition does not include photon detection efficiency or mirror reflectance. The simulation area depends on the method of ray-tracing used. For the parallel rays method the ray-traced photons were distributed over a square grid area of single side length $2.2 \times R_{\text{primary}}$ where R_{primary} is the radius of the primary mirror, thus $A_{\text{simulation}} = (2.2 \times R_{\text{primary}})^2$. For the random cone method the simulation area is defined by the cone thus $A_{\text{simulation}} = \pi\,(1.1 \times R_{\text{primary}})^2 \cos\theta_{\text{field}}$.

Using the definitions outlined above, Fig. 6 illustrates the derived effective collection area for a single SST-GATE telescope. For an on-axis observation, adding the structural components to the computational model results in a decrease in the effective collection area (for a single rotation angle) from ~9.2 m^2 to ~8.1 m^2. Thus with the key shadowing components included in the computational model, the SST-GATE effective collection area is expected to be $A_{\text{effective}} \approx 8.1$ m^2 for on-axis observations decreasing to $A_{\text{effective}} \approx 7.3$ m^2 toward the FOV edge. Varying the source distance changes the effective collection area by less than 2%.

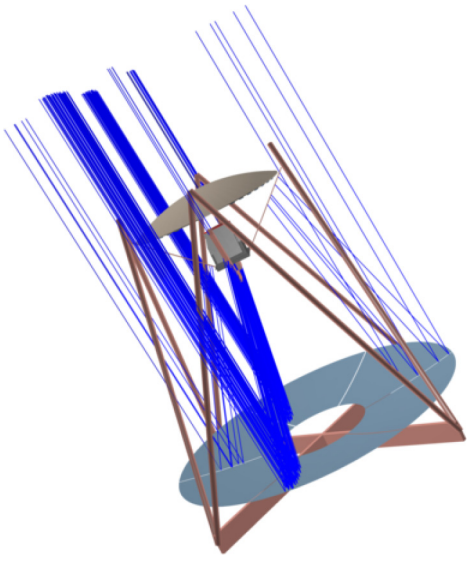

Fig. 7. Shown here is a fraction (5%) of the rays simulated (solid blue lines) that are stopped by the camera support trusses and the camera support bars for an off-axis ($\theta_{\text{field}} = 4^\circ$) observation. (For interpretation of the references to color in this figure legend, the reader is referred to the web version of this article.)

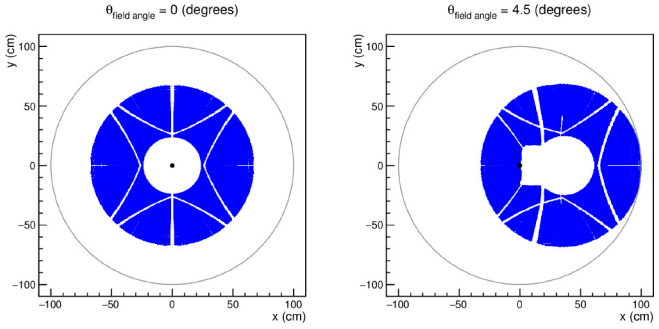

Fig. 8. Shown here are the ray-traced photons as they arrive at the surface of the secondary mirror for an on-axis observation (left panel) and an off-axis observation (right panel). Shadowing from the secondary mirror, the secondary mirror support masts, the camera support trusses and the camera support bars is clearly visible in both panels. Shadowing from the camera housing envelope is only visible when observing at large field angles ($\theta_{\text{field}} > 2^\circ$). The black dot denotes the center-point of the secondary mirror and the solid gray line shows the secondary mirror circumference.

One major advantage of using *ROBAST* to conduct the SST-GATE optical performance simulations, is that it is possible to keep a record of all the light rays that are stopped by single or multiple telescope components included in the 3D computational model. Using the parallel ray-tracing method we determined both the fraction of light rays stopped by a specific telescope component as well as the fraction of light rays lost at the telescope focal plane due to shadowing caused by these components. Fig. 7 illustrates a sample (5%) of the traced light rays being stopped by the SST-GATE camera support trusses and the camera support bars for an off-axis ($\theta_{\text{field}} = 4^\circ$) observation.

The SST-GATE shadowing is dominated by the secondary mirror that is half the diameter of the primary mirror. This causes a light loss of ~25%. As already mentioned additional shadowing arises from the support mechanics (e.g. masts and trusses) as well as the camera. The camera casts a shadow onto the secondary mirror for rays coming from the primary mirror. For most field angles this area coincides with the secondary mirror shadow on the primary mirror, and is only visible on the secondary mirror at large field angles. Fig. 8 illustrates the shadowing effects seen on the

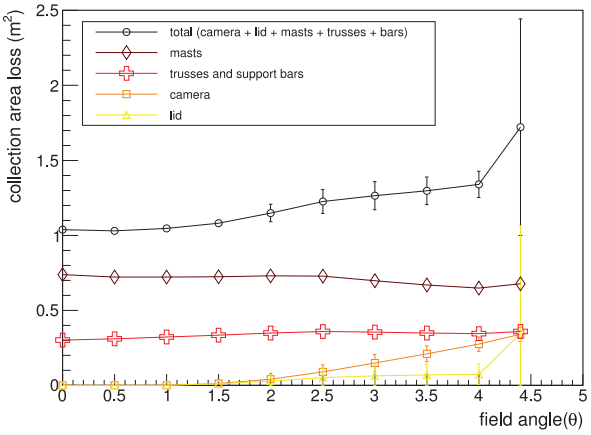

Fig. 9. Shown here is the expected loss in effective collection area as a function of field angle that results when the shadowing components (i.e. masts, trusses and camera envelope) are added to the computational model. These are mean values averaged over all ϕ angles analyzed. The total expected loss in effective collection area (black line with open circles) is calculated by summing the expected losses from each of the individual shadowing components. The error bars show the standard deviation for each field angle. At very large field angles ($\theta_{\text{field}} > 4°$) the large error bars are due to the increased shadowing seen when rays are traced from the lid-side of the camera ($\phi_{\text{rotation}} = 270°$).

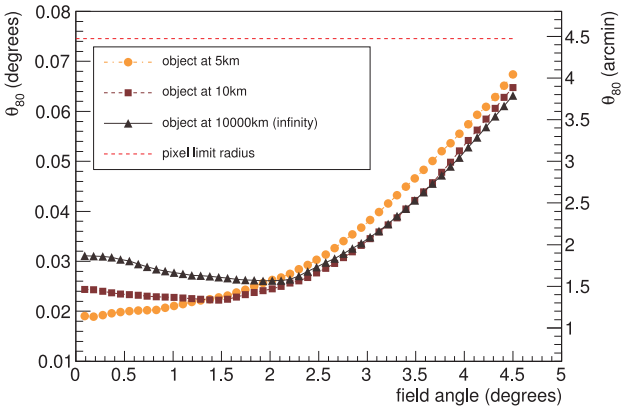

Fig. 10. Shown here are the encircled θ_{80} values derived (using *Zemax*) as a function of field angle for the SST-GATE telescope for an object at a distance from the telescope of 5 km (yellow filled-circles), 10 km (maroon filled-squares) and 10000 km (black filled-triangles, can be considered as infinity). This illustrates that the derived θ_{80} values change by < 1 arcmin for all field angles and between the different object distances analyzed. Thus, for the observation of Cherenkov air showers, there is no significant change in the image quality along the depth of field. (For interpretation of the references to color in this figure legend, the reader is referred to the web version of this article.)

surface of the secondary mirror as rays from the primary mirror are stopped for an on-axis observation ($\theta_{\text{field}} = 0°$) and an off-axis observation ($\theta_{\text{field}} = 4.5°$).

For each of the structural components included in the computational model it is possible to determine the total number of rays stopped as a function of field angle. Moreover, it is possible to determine the effective collection area change as a function of field angle that results from each of these shadowing components.

Parallel rays for 10 field angles $\theta_{\text{field}}(0°, 4.4°)$ and 8 rotation angles around the z-axis $\phi(0°, 360°)$ were traced and analyzed in order to determine the shadowing that results from the major SST-GATE components: the secondary support masts, the camera support trusses, the camera housing envelope and the camera lid envelope. The secondary mirror is a fundamental design characteristic of the SST-GATE telescope and is thus not considered to be a shadowing component that adversely affects the performance parameters like effective collection area. Fig. 9 shows the expected loss in effective collection area as a function of field angle that results when the shadowing components (i.e. masts, trusses and camera envelope) are added to the computational model.

For each telescope component, the shadowing contributions remain relatively stable for all field angles except the largest ($\theta_{\text{field}} = 4.4°$) analyzed. For field angles of $0° \leq \theta_{\text{field}} \leq 4°$ the total mean effective collection area loss is between 1 m^2 and 1.3 m^2. For an on-axis observation this is a similar loss (~11%) to that seen with current Davies–Cotton (DC) Cherenkov telescopes with ~5° FOV [21]. For the largest field angle analyzed $\theta_{\text{field}} = 4.4°$ the total mean effective collection area loss increases to ~1.7 m^2. The large standard deviation seen at this field angle is due to an increase in the number of rays that are stopped by the camera and lid when rays are traced from the lid-side direction of the camera ($\phi_{\text{rotation}} = 270°$).

The `final design` computational model was used for the shadowing analysis and does not include every detail of the telescope structure (as seen in Fig. 1). We do not expect the inclusion of these extra components to significantly affect the shadowing results shown here. Likewise, we do not see any increase in the overall shadowing from the components in the `final design` compared to those in the 2014 `design`. Instead we see a redistribution of the shadowing contribution between the masts and the trusses. This is evident by comparing Fig. 9 with [22] (Fig. 3 therein) which shows the shadowing contribution of the 2014 `design`.

3.3. Depth of field

An aspect of the telescope design we evaluated was the influence of the distance of an air shower with respect to the telescope. The SST-GATE optics were designed for an object distance of 10 km, but this is just an average value and while the distance decreases with increasing altitude of the observatory, it increases with zenith distance of the observation. To evaluate any change of the image quality we tested three separate models with an object distance of 5 km, 10 km and 10000 km (representing infinity) respectively. Fig. 10 shows that the derived θ_{80} values change by $<$ 1 arcmin for all field angles and between the different object distances analyzed. Thus, for the observation of Cherenkov air showers, there is no significant change in the image quality along the depth of field.

3.4. Plate scale distortion

In the final optical design, a certain residual aberration still remains due to a small variation of the plate scale with the field angle. A *Zemax* analysis of this effect shows that the distortion is of the barrel-type, meaning the image gets ~2.5%} larger at the field edge. Fig. 11 illustrates this effect which has to be taken into account to enable a precise trajectory estimate for the gamma-ray showers observed.

3.5. Photon time spread

The CTA design specifications for the SST stipulates that the telescope must focus light with an optical time spread of $<$ 1.5 ns. Using *ROBAST*, Fig. 12 illustrates the average time interval (as a function of field angle) between the arrival on the focal plane of the first and last ray-traced photon. The error bars show the standard deviation of the time-spread photons. As expected the photon time spread increases for large field angles as the photons travel

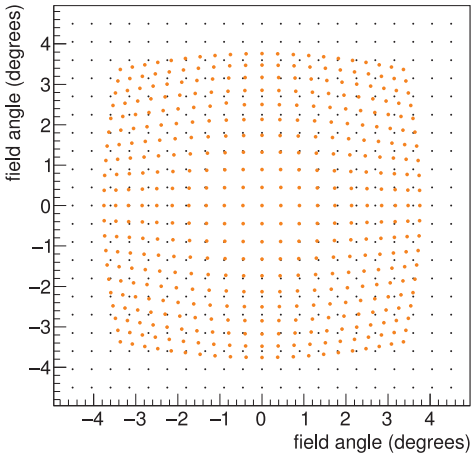

Fig. 11. Shown here is the barrel-type distortion seen for the SST-GATE optical design. This is seen when comparing the end-points of the traced rays on the focal plane for the non-distorted rays (black filled circles) and the distorted rays (yellow filled circles). For the purposes of illustration we have exaggerated the barrel-type distortion by making the effect 10 times stronger. (For interpretation of the references to color in this figure legend, the reader is referred to the web version of this article.)

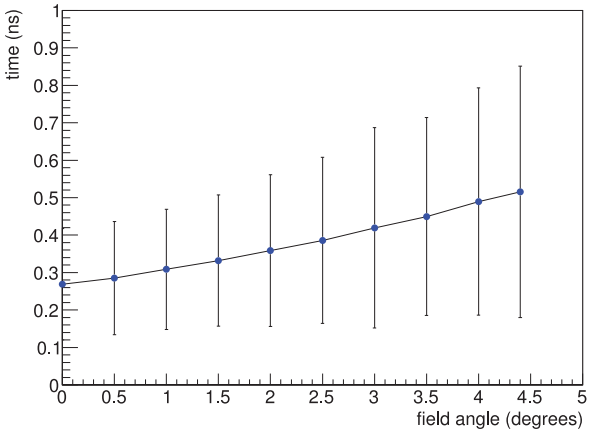

Fig. 12. Shown here is the average time interval (as a function of field angle) between the arrival on the focal plane of the first and last ray-traced photon. The error bars show the standard deviation of the photon arrival times for each field angle. This shows that the SST-GATE optical design meets the CTA time-spread requirements (which are standard deviation < 1.5 ns).

a longer path length through the telescope optics. These findings confirm that the SST-GATE optical design successfully meets the CTA time spread specifications.

4. Tolerance analysis

The preliminary SST-GATE design work was conducted with *Zemax* and included an analysis of the design's tolerances. In a second step we derived results with *ROBAST* for a single parameter tolerance analysis as well as a (more realistic) random tolerance analysis, in which all free parameters are allowed to vary at the same time. In addition, we also tested two parameters not studied with *Zemax*: the margin between the primary mirror petals and the mirror surface micro-roughness. The purpose of the tolerance analysis is to help guide a strategy for SST-GATE alignment procedures. The tolerance analysis was conducted prior to the SST-GATE telescope design update and the ray-tracing was done using the `2014 design` model. As already mentioned in

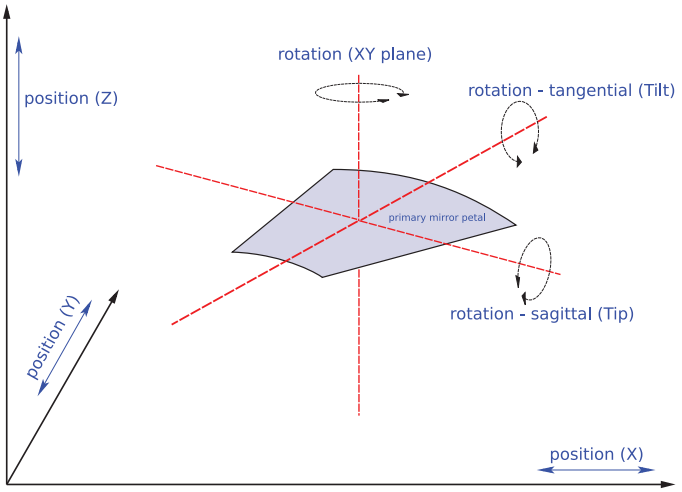

Fig. 13. Shown here is a sketch highlighting the position and rotation axes of a single primary mirror petal used for the tolerance analysis. The same translation and rotation definitions were used for the monolithic secondary mirror tolerance tests.

Table 2
The SST-GATE single parameter tolerances derived using *Zemax* (top section) and the new parameters tested using *ROBAST* (bottom section).

Test	Mirror	Axis	Range
Rotation	Primary	Sagittal (tip)	$-0.01^\circ \cdots +0.02^\circ$
—"—	—"—	Tangential (tilt)	$-0.01^\circ \cdots +0.01^\circ$
—"—	—"—	XY	$-0.14^\circ \cdots +0.12^\circ$
—"—	Secondary	Sagittal (tip)	$-0.1^\circ \cdots +0.08^\circ$
—"—	—"—	Tangential (tilt)	$-0.6^\circ \cdots +0.6^\circ$
—"—	—"—	XY	$-0.14^\circ \cdots +0.14^\circ$
Position	Primary	X (translation)	-5 mm $\cdots +5$ mm
—"—	—"—	Y (translation)	-3 mm $\cdots +3$ mm
—"—	—"—	Z (translation)	-5 mm $\cdots +5$ mm
—"—	Secondary	X (translation)	-5 mm $\cdots +5$ mm
—"—	—"—	Y (translation)	-2 mm $\cdots +2$ mm
—"—	—"—	Z (translation)	-1 mm $\cdots +1$ mm
Roughness	Primary	–	0.011°
—"—	Secondary	–	0.041°
—"—	Dual	–	0.013°
Margin	Primary	–	8 mm ... 12 mm

Section 3, when comparing the resulting θ_{80} values between the `final design` and the `2014 design` we see no significant change. Therefore our choice of computational model for the tolerance analysis (which only tests the θ_{80} values) should not significantly affect these results. Fig. 13 shows a sketch of a single primary mirror petal including the position and rotation axes used for this tolerance analysis work. The same translation and rotation definitions were used for the monolithic secondary mirror tolerance tests.

Table 2 highlights the *Zemax* derived tolerances for the SST-GATE optical model. Using *ROBAST*, these parameters and ranges were then tested in the single parameter tolerance analysis in order to keep the θ_{80} value within the pixel limit radius i.e. for 80% of the spot image photons to be contained within a single pixel.

Only the parameters which appear to have the greatest influence on the stability of θ_{80} will be discussed. These include the translation of the secondary mirror (and thus of the focal plane) in the z-direction, the tipping and tilting of the primary mirror petals and the mirror surface roughness.

The translation of the focal plane in the z-direction appears to significantly affect the resulting θ_{80} value. Fig. 14 shows that even

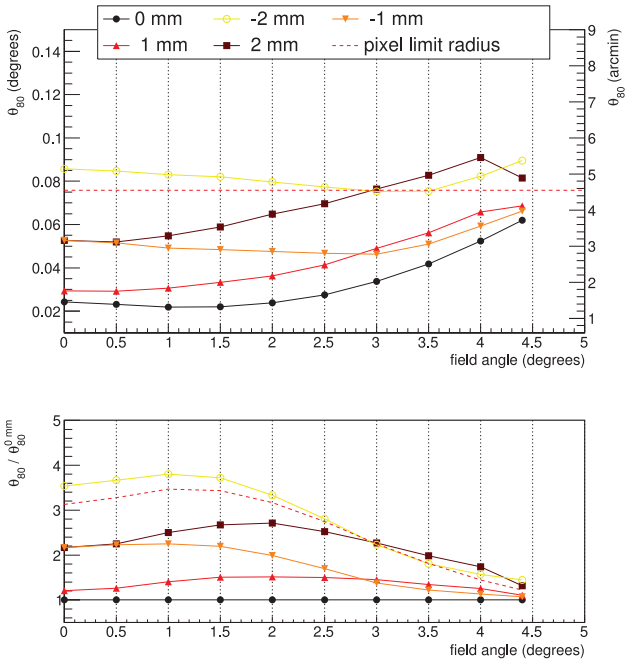

Fig. 14. Shown here is the encircled θ_{80} value derived as a function of field angle for different z-positions of the focal plane. It is obvious that even a small change in z-position has a significant effect on θ_{80}. The pixel limit radius is defined as the radius within which 80% of the spot photons would be contained within a single pixel.

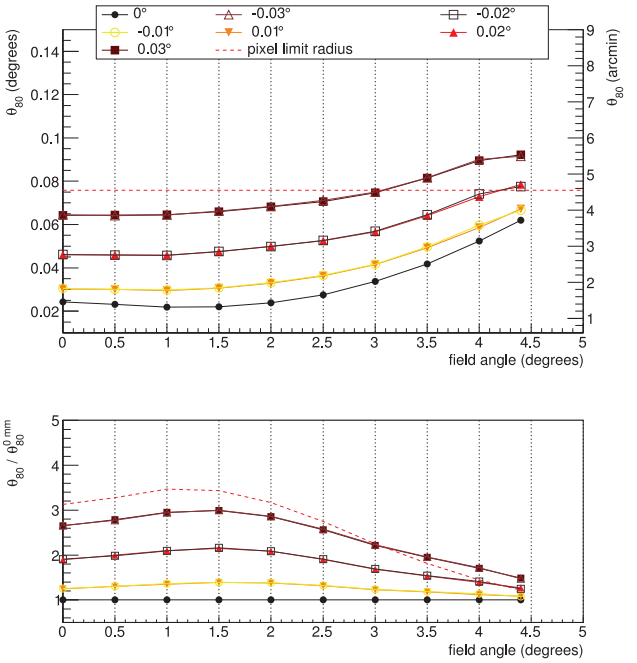

Fig. 15. Shown here is the encircled θ_{80} derived as a function of field angle for different tangential rotations of the primary mirror petals. Tilting in either direction has a symmetric effect on θ_{80}, and it appears that in order to stay within the pixel limit radius for all field angles, tilting of the primary petals should be kept within the range $-0.01^\circ \leq \theta \leq 0.01^\circ$.

a small change (∼2 mm) in the focal plane z-position can lead to a significant deterioration of the derived θ_{80} value. Additional tolerance tests were conducted for the z-position of the primary mirror petals and the z-position of the secondary mirror. The θ_{80} value appears relatively stable within the limits shown in Table 2 for changes in primary petal z-positions, which is expected as only 1/6th of the mirror contributes to the deterioration of the encircled energy. However, θ_{80} is sensitive to changes in the z-position of the primary (i.e. all petals) and secondary mirrors. When altering the secondary mirror z-position and keeping all other values in their ideal position this affects two separation distances; the separation distance between primary mirror and the secondary mirror and the separation distance between the secondary mirror and the focal plane. The dominant effect is the change in distance between the secondary mirror z-position and the focal plane. In this respect the mechanical design is based on a priority link between the secondary mirror and the focal plane, and the allowed tolerance for the secondary mirror z-position relative to the focal plane is smaller to a maximum deviation of -1 mm $\leq z \leq 1$ mm as reflected in Fig. 14.

In the preliminary tolerance analysis conducted with *Zemax*, the SST-GATE spot image was found to be sensitive to rotational movement about 2 axes of the primary mirror petals; sagittal rotation or tipping of the petals toward and away from the optical axis and tangential rotation or tilting of the petals on their sides (both shown in Fig. 13).

The sensitivity of θ_{80} to tilting and tipping of the primary mirror petals is shown in Fig. 15. This illustrates that for θ_{80} to stay within the pixel limit radius for all field angles, tilting of the petals (all in the same way) should be kept within the range $-0.01^\circ \leq \theta \leq 0.01^\circ$.

Likewise Fig. 16 also illustrates that in order for the θ_{80} value to stay within the pixel limit radius for all field angles, tipping of the primary mirror petals (all in the same way) should be kept within the range $-0.01^\circ \leq \theta \leq 0.02^\circ$.

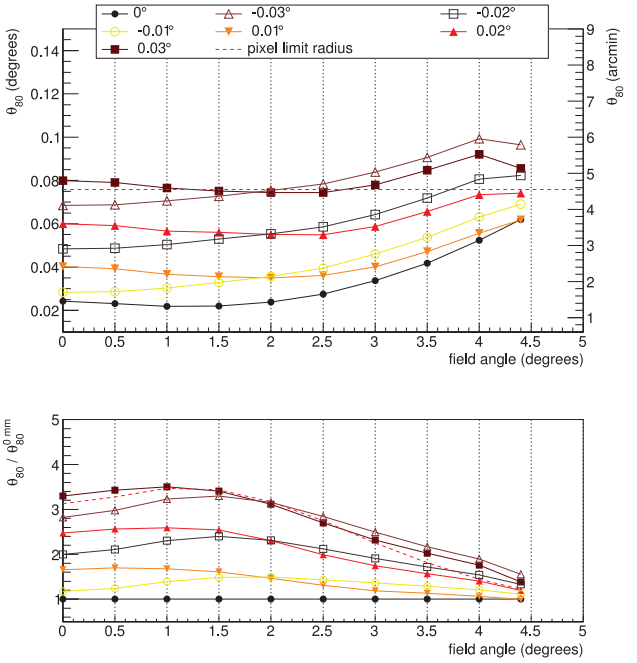

Fig. 16. Shown here is the encircled θ_{80} derived as a function of field angle for different sagittal rotations of the primary mirror petals. Tipping inward toward the optical axis has a greater effect on θ_{80} compared to an outward direction. For θ_{80} to remain within the pixel limit radius for all field angles, it appears that tipping of the primary mirror petals should be kept within the range $-0.01^\circ \leq \theta \leq 0.02^\circ$.

Using the *ROBAST* library, it is possible to perform a tolerance analysis of the SST-GATE mirror quality in a very simple approach that does not treat explicitly the actual mirror surface structure and the wavelength dependence of the diffusion it causes. Typically, for Cherenkov telescopes the mirror surface deviation from the ideal shape ("form deviation"), which is much larger than the

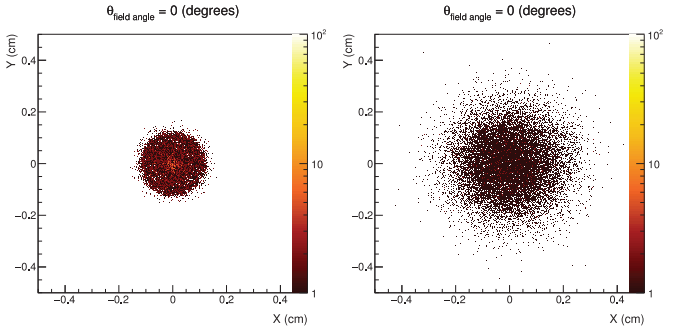

Fig. 17. Shown here are the focal plane spot images for an on-axis observation ($\theta_{\text{field}} = 0^{\circ}$) using different values for the mirror roughness parameter. The left panel shows the spot image with a mirror roughness of 0.001° for both the primary and secondary mirrors. The right panel shows the spot image with the mirror roughness parameter (for both the primary and secondary mirrors) increased by an order of magnitude to 0.01°. These plots illustrate how an increase in the roughness parameter results in the smearing of the focal plane spot image. The plate scale is 39.6 mm/° (see Table 1).

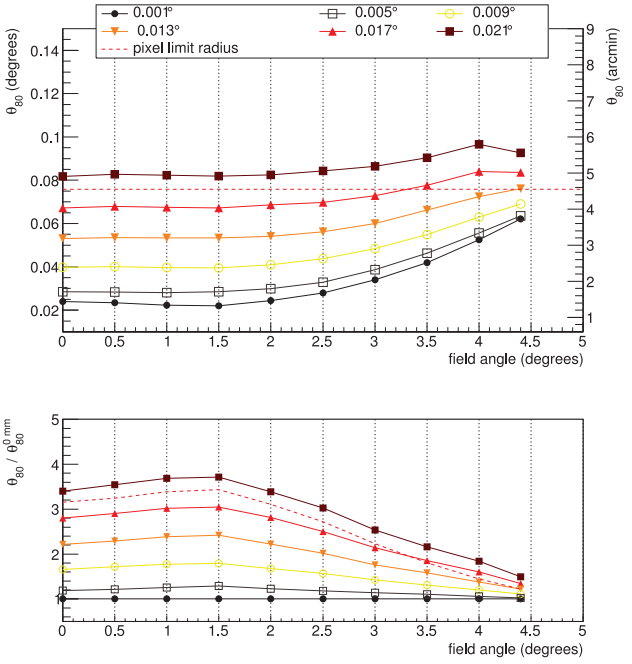

Fig. 18. Shown here is the encircled θ_{80} derived as a function of field angle for a selection of different mirror surface roughness values ranging from 0.001° to 0.021°. The value of θ_{80} shown here is derived assuming both the primary and secondary mirrors are manufactured with the same surface roughness. It appears that a surface roughness better than 0.013° results in θ_{80} staying within the pixel limit radius for all field angles except the largest.

incident wavelengths, is the dominant effect in determining the optics performance. Such "form deviations" can have an impact on the PSF, but the study of their impact is beyond the scope of this work. In addition, one has to account for the irregularities of the mirror surface at size scales close to the wavelength of the incident light. This "surface roughness" leads to the scattering of a fraction of the incident photons. For simplicity, we approximate the form deviation and the scattering by a single Gaussian. Within *ROBAST* this reflection angle distribution (which we will now simply refer to as roughness) is simulated as a two-dimensional Gaussian such that when the roughness is equivalent to 1°, the projected one-dimensional angular distribution around the ideal reflection angle will be a Gaussian of 1° width ($\sigma_{\text{roughness}} = 1^{\circ}$). Fig. 17 shows that by increasing the mirror roughness this results in a smearing of the spot image at the focal plane. The left panel shows the spot image for an on-axis ($\theta_{\text{field}} = 0^{\circ}$) observation with a mirror roughness of 0.001° set for both the primary and secondary mirrors . The right panel shows the same spot for an on-axis observation, but with the mirror roughness parameter (for both the primary and secondary mirrors) increased by an order of magnitude to 0.01°.

Fig. 18 illustrates the sensitivity of θ_{80} to different roughness values for both the primary and secondary mirrors. Due to the longer path length for each ray, θ_{80} is more sensitive to changes in the roughness of the primary mirror compared to that of the secondary mirror. However, it is assumed that the quality of both mirrors will be identical and thus the single parameter tolerance analysis shown here was conducted for both mirrors simultaneously. It appears that if all telescope elements are perfectly aligned, then an SST-GATE mirror roughness resulting in a diffusion angle width of 0.013° produces a θ_{80} value within the pixel limit radius for all field angles except the largest analyzed. However, it should be noted that even at this roughness value θ_{80} at a field angle of 1.5° is roughly a factor of 2.4 worse than a mirror which produces an order of magnitude smaller diffusion angle.

A limitation of the single parameter tolerance test is that one has to assume all other parameters are fixed at their optimal value. In practice, this may not be the case and θ_{80} may be very sensitive to a combination of misalignments. Thus a random tolerance test was also conducted for the SST-GATE telescope using the findings of the single tolerance analysis to help define the parameter ranges. From these parameter ranges a value was selected randomly for all the telescope's degrees of freedom being analyzed. Assuming that the real misalignments of the telescope components are normally distributed about their ideal positions, the parameter values were randomly selected using a Gaussian distribution.

Table 3 highlights the new parameter ranges using input from the single parameter tolerance analysis (see Table 2). Two random tolerance tests were conducted: the first, called a "broad sigma" test, required that 99.73% (3σ) of the randomly selected parameter values fall within the tolerance range defined from the single parameter analysis, and the second, called a "narrow sigma" test, required 99.73% of the randomly selected parameters to fall within a manually adjusted, smaller range (cf. last column of Table 3), resulting in a θ_{80} distribution closer to the ideal one. Table 3 also highlights the mean (μ) and 3σ values used to create the normal distributions for the random selection of the parameters in both the broad and narrow tests. The roughness value was fixed for both mirror surfaces as this is not expected to change in the short term. For both tests the average θ_{80} values fall within the pixel limiting radius, but the standard deviation of the broad test results exceeds the pixel limit at the largest field angles (above 3.5°).

Fig. 19 shows the mean θ_{80} as a function of field angle (top panel) obtained for 250 random tolerance parameter selections and the error bars show the standard deviation. The average θ_{80} value derived using the broad sigma test values (solid yellow line with open squares) and the average θ_{80} value derived using the narrow sigma test values (solid maroon line with open upward triangles) are compared here with the ideal θ_{80} value (solid black line with open circles) derived for a perfectly aligned telescope system (see Fig. 5). The dashed horizontal red line shows the pixel limit radius. The bottom panel shows the residual values calculated by dividing $\theta_{80}^{\text{sigmatest}}/\theta_{80}^{\text{ideal}}$. The broad sigma test results in θ_{80} values that are on average 1.8 times worse than the ideal θ_{80} value for all field angles.

Table 3
SST-GATE random tolerance analysis parameters.

Test	Mirror	Axis	Probed Range	μ	$3\sigma_{\text{broad}}$	$3\sigma_{\text{narrow}}$
Rotation	Primary	Sagittal	$-0.02^\circ \cdots +0.02^\circ$	$\mu = 0^\circ$	0.02°	0.01°
——"——	——"——	Tangential	$-0.02^\circ \cdots +0.02^\circ$	$\mu = 0^\circ$	0.02°	0.01°
——"——	——"——	XY	$-0.12^\circ \cdots +0.12^\circ$	$\mu = 0^\circ$	0.12°	0.02°
——"——	Secondary	Sagittal	$-0.05^\circ \cdots +0.05^\circ$	$\mu = 0^\circ$	0.05°	0.02°
——"——	——"——	Tangential	$-0.05^\circ \cdots +0.05^\circ$	$\mu = 0^\circ$	0.05°	0.02°
——"——	——"——	XY	$-0.14^\circ \cdots +0.14^\circ$	$\mu = 0^\circ$	0.14°	0.02°
Position	Primary	X	-5 mm $\cdots +5$ mm	$\mu = 0$ mm	5 mm	1 mm
——"——	——"——	Y	-3 mm $\cdots +3$ mm	$\mu = 0$ mm	3 mm	1 mm
——"——	——"——	Z	-5 mm $\cdots +5$ mm	$\mu = 0$ mm	5 mm	1 mm
——"——	Secondary	X	-5 mm $\cdots +5$ mm	$\mu = 0$ mm	5 mm	1 mm
——"——	——"——	Y	-2 mm $\cdots +2$ mm	$\mu = 0$ mm	2 mm	1 mm
——"——	——"——	Z	-1 mm $\cdots +1$ mm	$\mu = 0$ mm	1 mm	0.5 mm
Roughness	Dual	-	0.001°	-	-	-
Margin	Primary	-	8 mm ... 12 mm	$\mu = 10$ mm	2 mm	2 mm

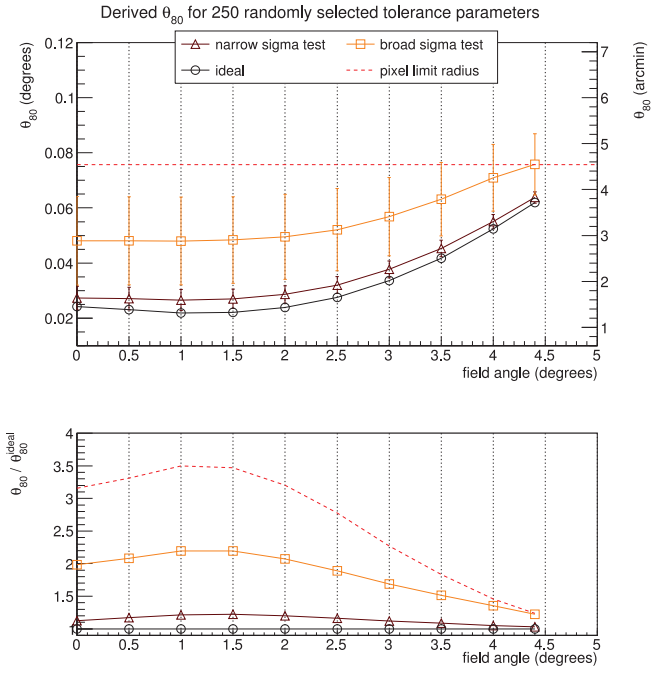

Fig. 19. The average θ_{80} value as a function of field angle (top panel) derived using parameters that were randomly selected from a normal distribution with broad sigma values (solid orange line with open squares) and narrow sigma values (solid maroon line with open upward triangles). For comparison, the ideal θ_{80} value derived for a perfectly aligned telescope system and shown in Fig. 5, is also shown here (solid black line with open circles). The θ_{80} value is averaged for 250 random parameter selections and the error bars show the standard deviation. The pixel limit radius is indicated by the horizontal red dashed line. The bottom panel shows the residual values calculated by dividing $\theta_{80}^{\text{sigmatest}}/\theta_{80}^{\text{ideal}}$. (For interpretation of the references to color in this figure legend, the reader is referred to the web version of this article.)

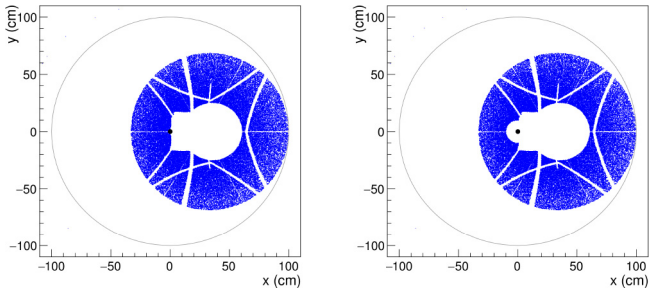

Fig. 20. Shown here are the ray-traced photons as they arrive at the surface of the secondary mirror with no central hole (left panel) and with a 100 mm radius central hole (right panel). Both panels show the photons ray-traced for an off-axis ($\theta = 4.4^\circ$) observation. The shadowing from the secondary mirror support masts, the camera support trusses, the camera support bars and the camera housing envelope is clearly visible in both panels. The inclusion of a central hole to the secondary mirror is clearly visible in the right panel. The black dot denotes the centerpoint of the secondary mirror and the solid gray line shows the secondary mirror circumference.

5. Secondary hole analysis

An additional optical performance test of the general SST-GATE design was an analysis of the effects that result from introducing a hole or dead space at the center of the secondary mirror. The reason for doing this is to determine whether it is possible to fit additional instrumentation into this space that could be used for telescope pointing and alignment calibration.

An opaque circular mask, which will be called a central hole for simplicity, was added to the center of the secondary mirror in *ROBAST*. Ray-tracing using the random cone method was performed, and the hole radius was increased in steps of 50 mm from 0 mm to 200 mm. Fig. 20 illustrates the ray-traced photons as they arrive at the surface of the secondary mirror with no central hole (left panel) and with a 100 mm radius central hole (right panel). Both panels show the photons ray-traced for an off-axis ($\theta = 4.4^\circ$) observation where the effect is largest. The shadowing from the secondary mirror support masts, the camera support trusses and the camera housing envelope can be seen in both panels. The inclusion of a central hole to the secondary mirror is clearly visible in the right panel.

The θ_{80} value as a function of field angle was derived for the different secondary mirror central hole radii. Fig. 21 illustrates θ_{80} (top panel) as a function of field angle for the different central hole radii. The bottom panel shows the residuals ($\theta_{80}^{r_{\text{hole}}}/\theta_{80}^{r_{\text{hole=0mm}}}$) from the ideal θ_{80} value i.e. no central hole (solid black line, filled circles). It is clear that, for the radii we tested, θ_{80} is not significantly sensitive to the addition of a hole in the center of the secondary mirror.

Using the method described in Section 3.2, the effective collection area as a function of field angle was also calculated for secondary mirrors with different central hole radii as shown in Fig. 22 (top panel). The bottom panel shows the residuals ($A_{\text{eff}}^{r_{\text{hole}}}/A_{\text{eff}}^{r_{\text{hole=0mm}}}$) from the ideal effective collection area i.e. no central hole (solid black line filled circles). It is clear that the effective collection area is sensitive to the addition of a central hole at the center of the secondary mirror for $\theta \geq 1^\circ$. It appears that a hole up to a

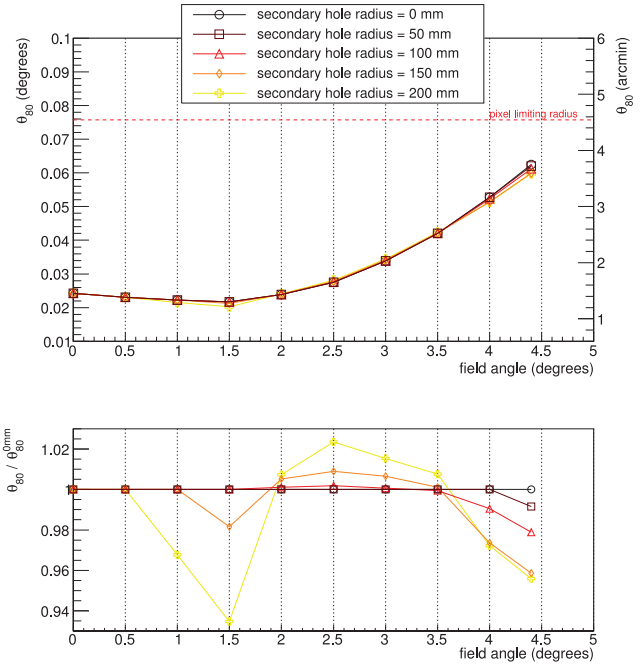

Fig. 21. Shown here are the derived encircled θ_{80} values (top panel) as a function of field angle for different hole radii on the secondary mirror. Also shown are the residuals (bottom panel) from the ideal θ_{80} i.e. no central hole (solid black line filled circles).

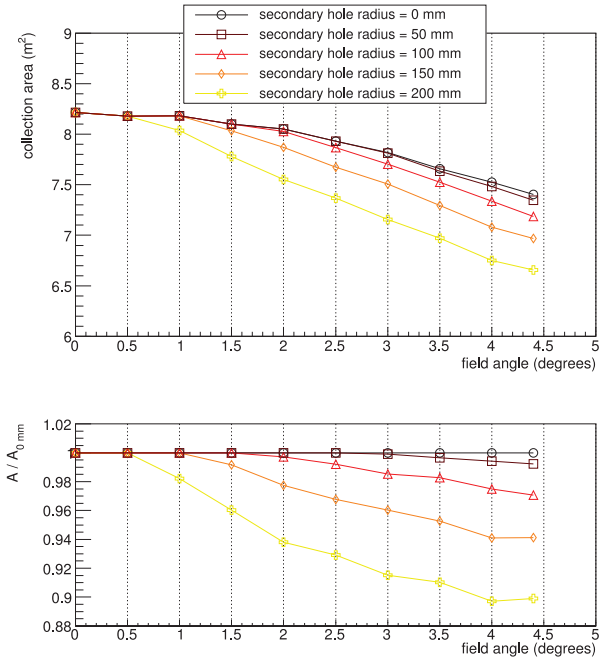

Fig. 22. Shown here are the derived effective collection area values (top panel) as a function of field angle for different secondary mirror hole radii. Also shown are the residuals (bottom panel) from the ideal effective collection area i.e. no central hole (solid black line filled circles). It is clear that the effective collection area is sensitive to the addition of a hole in the center of the secondary mirror for $\theta \geq 1°$.

radius 150 mm is feasible, as even with a hole of this size, the effective collection area residual remains above ~94% for all field angles.

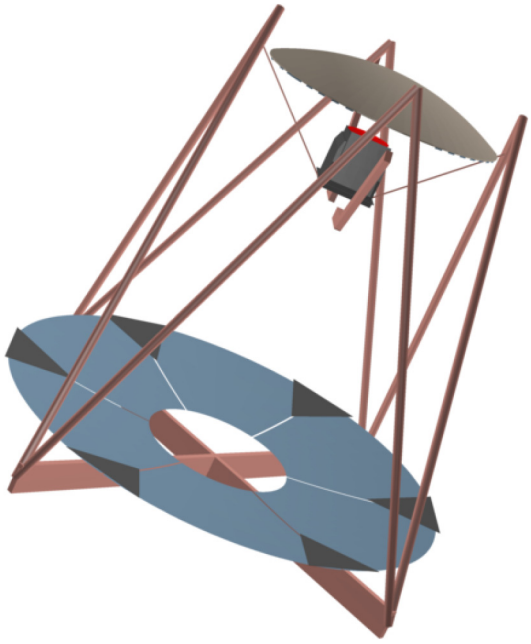

Fig. 23. Shown here is a computational model of the SST-GATE telescope `final design` which includes triangular masks overlaid on top of the primary petals in order to simulate the effect of trimming the proposed petals.

6. Primary mirror petal analysis

The SST-GATE prototype telescope [12] constructed at the Paris Observatory has primary mirror petals that are smaller than those of the GCT proposed for the CTA [23]. This is due to the fact that the construction of a single prototype telescope required a compromise solution for the primary mirror petals due to size constraints of existing mirror molds. If the GCT design is chosen for mass production, the cost for a larger, dedicated mirror mold will be acceptable.

A study was conducted in order to determine how smaller primary mirror petals would impact the θ_{80} value and the effective collection area. To simulate the impact of trimmed petals this study implements a very simple approach. Triangular masks are overlaid above the proposed petals as if the petals themselves were trimmed. Fig. 23 illustrates the SST-GATE `final design` computational model with the masks overlaid.

Using the random cone ray tracing method, Fig. 24 shows the spot images generated on the ideal focal plane for different field angles. Trimming or masking the primary mirror petals results in spot images with a flower type shape. Essentially the image quality deteriorates and this effect is exaggerated as the field angle increases.

The cyan-colored circles in Fig. 24 show the θ_{80} values fitted to the spot images for each of the field angles analyzed. Despite the image deterioration seen, the effect on θ_{80} is negligible. Using these spot images, Fig. 25 illustrates the derived θ_{80} value as a function of field angle for the SST-GATE prototype telescope (solid red line with open squares) with trimmed primary mirror petals. Using the encircled method, θ_{80} does not significantly deteriorate relative to the θ_{80} value calculated for the ideal SST-GATE telescope proposed (solid black line with open circles). Trimming the primary mirror petals of the prototype telescope does not cause any deterioration of the θ_{80} values across the telescope FOV.

Fig. 26 illustrates the effective collection area calculated for the SST-GATE prototype with trimmed primary mirror petals. As

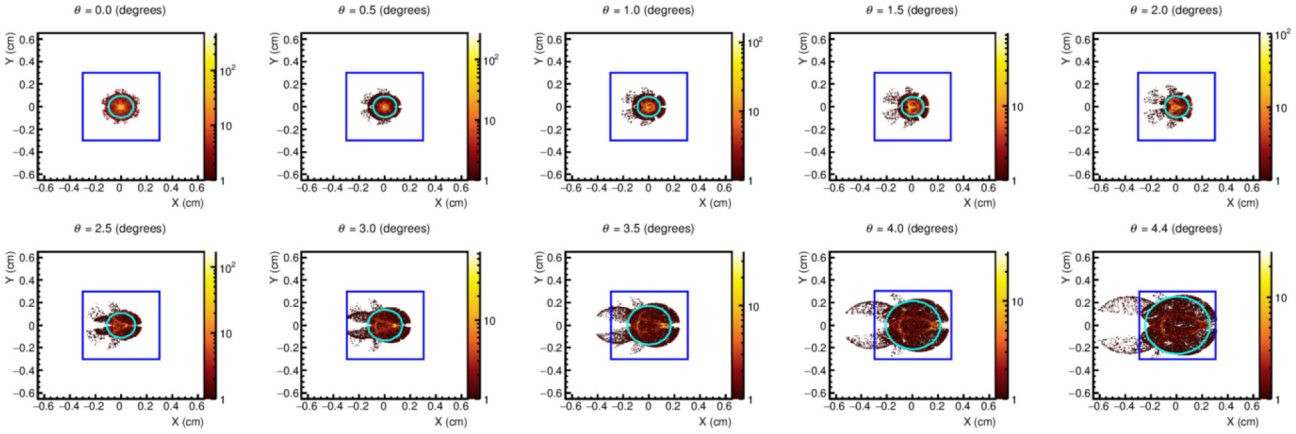

Fig. 24. Shown here are the spots generated on the ideal focal plane of the SST-GATE prototype telescope. Each panel is a 1.3 cm × 1.3 cm area on the focal plane centered on the spot center of mass generated for a given field angle (θ). The color scale illustrates the photon number and the box (solid blue line) illustrates the expected camera pixel size (6 mm × 6 mm). The circle (solid cyan line) shows the derived encircled θ_{80} (see Section 3.1) which is defined as the radius within which 80% of the photons lie. Trimming or masking the primary mirror petals results in the deterioration of the spot image. This effect becomes more noticeable as the field angle increases. As before (see Fig. 4) the center of the camera is to the left for angles > 0°. (For interpretation of the references to color in this figure legend, the reader is referred to the web version of this article.)

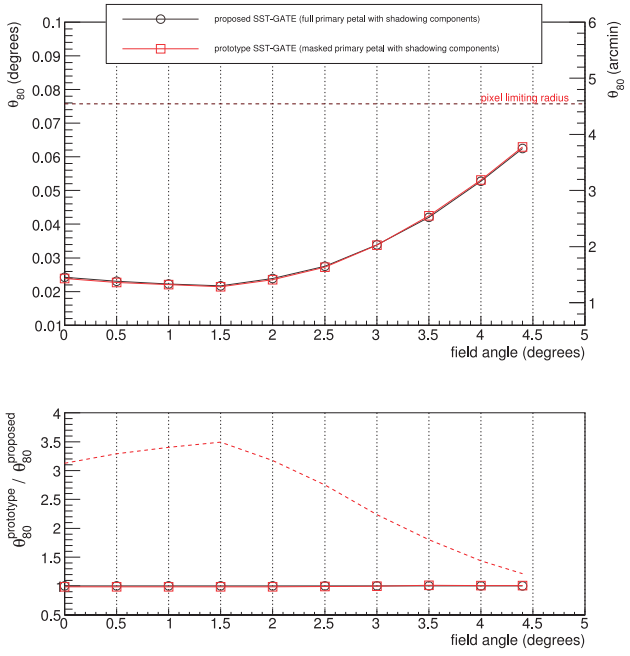

Fig. 25. The top panel shows the derived θ_{80} values as a function of field angle for the SST-GATE prototype (solid red line with open squares) using a mask to simulate the trimmed primary mirror petals. As seen here, trimming the primary mirror petals of the prototype telescope does not cause any deterioration of the θ_{80} values across the telescope FOV. (For interpretation of the references to color in this figure legend, the reader is referred to the web version of this article.)

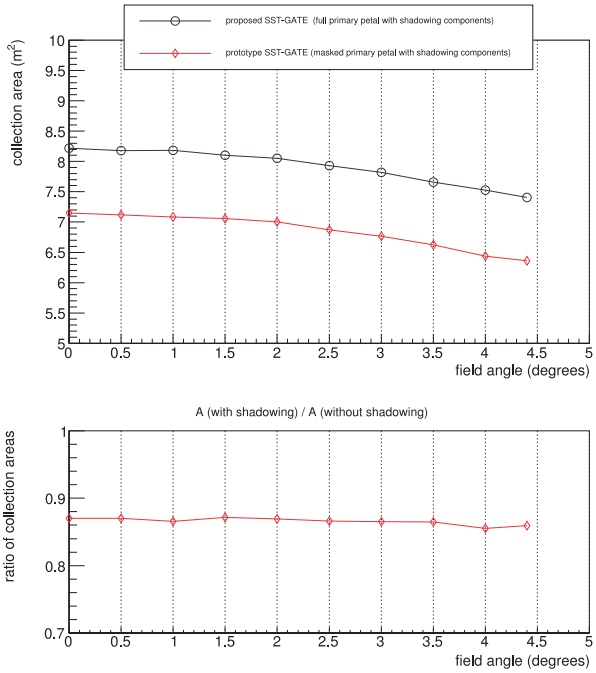

Fig. 26. The top panel shows the effective collecting area as a function of field angle for a single SST-GATE prototype telescope (solid red line with open diamonds) using a mask to simulate the trimmed primary mirror petals. The effective collection area is smaller relative to the effective collection area calculated for ideal SST-GATE telescope proposed (solid black line with open circles). As shown in the bottom panel, trimming the primary petals results in an effective collection area that is approximately ∼ 15% smaller for all field angles. (For interpretation of the references to color in this figure legend, the reader is referred to the web version of this article.)

the mask decreases the mirror surface area this has a direct impact on the effective collection area of the telescope and hence the effective collection area of the SST-GATE prototype (solid red line with open diamonds) is smaller relative to the effective collection area calculated for the ideal SST-GATE telescope proposed (solid black line with open circles). The effective collection area for the prototype is ∼15% smaller for all field angles analyzed.

7. Conclusions

In conclusion this work highlights some significant findings to be used in the continued development of the SST-GATE prototype telescope, and hence GCT proposed for the CTA. For all field angles the ideal encircled θ_{80} is smaller than the size of the camera pixels under consideration, leading to an optimal resolution of the air shower image on the camera. It is also shown that the

very good θ_{80} results presented in this paper which were produced using the *ROBAST* software are in excellent agreement with independent analysis conducted using different ray-tracing software, *sim_telarray* and *Zemax*.

Furthermore, we have studied for the first time the expected loss in the effective collection area for the SST-GATE telescope due to the telescope's shadowing components such as the secondary mirror support masts, the camera support trusses and the camera housing envelope including the camera lid. For an on-axis observation we see the shadowing results in the effective collection area decreasing by approximately 1 m^2. Reducing the shadowing from the additional components (which is at a similar level to that seen with current DC telescopes for on-axis observations) is unlikely to significantly improve the effective collection area performance relative to the cost of making any such improvements.

In addition, the results of a first extensive tolerance analysis highlighted in this paper show the need to carefully control certain parameters which greatly influence the stability of θ_{80}, especially the secondary mirror z-position, and the tip and tilt rotations of both the primary and secondary mirrors. For example the knowledge of the separation distance between the secondary mirror and the focal plane is required to sub-millimeter precision and thus there is a need for innovative instrumentation that will enable this to be easily, cost effectively and precisely monitored.

This paper also highlights that it is feasible to use a small circular area at the center of the secondary mirror, which is foreseen to be equipped with instrumentation for calibration and pointing accuracy measurement.

Concerning the prototype telescope, we have investigated the effect of reducing the size of the primary mirror petals. Such a reduction helps to significantly reduce the costs associated with constructing a single SST-GATE prototype while still meeting the CTA specifications. However this comes at the cost of poorer image quality (particularly for large offsets) and light collection efficiency for all field angles.

Finally, all of the SST-GATE optical performance simulation results shown in this paper have helped to optimize the technical trade-off required with the construction of the SST-GATE prototype [24]. A number of additional alignment and pointing studies for the SST-GATE telescope are still in progress and the intention is to publish these at a later date.

Acknowledgments

The authors would like to acknowledge the support provided by members of the SST-GATE teams of LUTH and GEPI at the Observatoire de Paris as well as colleagues at Durham University, the University of Liverpool and the University of Leicester. Particular mention should be made of Konrad Bernlöhr for developing and making available the *sim_telarray* software. Finally, the authors would like to acknowledge the financial support received from Convention 12008764 Région Ile-de-France et Observatoire de Paris, programme 2012 du DIM-ACAV. A. O. was supported by a grant-in-aid for JSPS Fellows and the optical design work of J.S. has been supported by STFC grant ST/J003646/1. Data files and software used for this research can be accessed online at https://github.com under the SST-GATE repository.

References

[1] B. Acharya, et al., Introducing the CTA concept, Astropart. Phys. 43 (3) (2013) 3–18.
[2] K. Bernlöhr, et al., Monte Carlo design studies for the Cherenkov Telescope Array, Astropart. Phys. 43 (2013) 171–188.
[3] T. Montaruli, G. Pareschi, T. Greenshaw, The small size telescope projects for the Cherenkov Telescope Array, in: Proceedings of 34th International Cosmic Ray Conference, 2015.
[4] J. Davies, E. Cotton, Design of the quartermaster solar furnace, J. Solar Energy Sci. Eng. 1 (1957) 16.
[5] R. Moderski, et al., 4 m Davies–Cotton telescope for the Cherenkov Telescope Array, in: Proceedings of 33rd International Cosmic Ray Conference, 2013. URL arXiv:1307.3137 [astro-ph.IM]
[6] K. Schwarzschild, Untersuchungen zur geometrischen Optik II, Astronomische Mittheilungen der Königlichen Sternwarte zu Göttingen 10 (1905) 1.
[7] A. Zech, et al., SST-GATE: a dual mirror telescope for the Cherenkov Telescope Array, in: Proceedings of 33rd International Cosmic Ray Conference, 2013. arXiv:1307.3035 [astro-ph.IM]
[8] G. Pareschi, et al., A dual-mirror small size telescope for the Cherenkov Telescope Array, in: Proceedings of 33rd International Cosmic Ray Conference, 2013. URL arXiv:1307.4962 [astro-ph.IM]
[9] V. Vassiliev, S. Fegan, P. Brousseau, Wide field aplanatic two-mirror telescopes for ground-based gamma-ray astronomy, Astropart. Phys. 28 (1) (2007) 10–27. URL http://www.sciencedirect.com/science/article/pii/S0927650507000527.
[10] M. Daniel, et al., A compact high energy camera for the Cherenkov Telescope Array, in: Proceedings of 33rd International Cosmic Ray Conference, 2013. URL arXiv:1307.2807 [astro-ph.IM]
[11] A. De Franco, et al., The first GCT camera for the Cherenkov Telescope Array, in: Proceedings of 34th International Cosmic Ray Conference, 2015. arXiv:1509.01480v1 [astro-ph.IM]
[12] D. Dumas, et al., SST-GATE telescope: an innovative dual-mirror prototype for the Cherenkov Telescope Array, in: Proceedings of SPIE, 9145, 91452Y, 2014.
[13] J.-L. Dournaux, et al., Performance of the Mechanical Structure of the SST-2M GCT Proposed for the Cherenkov Telescope Array, in: Proceedings of 34th International Cosmic Ray Conference, 2015. arXiv:1508.06415v1 [astro-ph.IM]
[14] Observatoire de Paris, URL http://www.obspm.fr/?lang=en.
[15] J.-L. Dournaux, et al., Mechanical design of SST-GATE: a dual mirror telescope for the Cherenkov Telescope Array, in: Proceedings of SPIE, 9151, 915102, 2014.
[16] J. Pope, Optical performance criteria for telescope tube design, in: R.M. West (Ed.), Proceedings of Large Telescope Design, ESO/CERN Conference, ESO Library ML 180/79, 1971, pp. 299–311.
[17] R. Brun, F. Rademakers, ROOT - An Object Orientated Data Analysis Framework, Proc. AIHENP'96 Workshop, Nucl. Inst. & Meth. in Phys. Res. A 389 (1997) 81–86. URL http://root.cern.ch.
[18] A. Okumura, K. Noda, C. Rulten, ROBAST: development of a ROOT-based ray–tracing library for cosmic-ray telescopes and its application in the Cherenkov Telescope Array, Astropart. Phys. 76 (2016) 38–47.
[19] The Zemax Software, URL http://www.zemax.com.
[20] K. Bernlöhr, Simulation of imaging atmospheric Cherenkov telescopes with CORSIKA and sim_telarray, Astropart. Phys. 30 (3) (2008) 149–158.
[21] K. Bernlöhr, et al., The optical system of the H.E.S.S. imaging atmospheric Cherenkov telescopes. Part I: layout and components of the system, Astropart. Phys. 20 (2003) 111–128.
[22] T. Armstrong, et al., Monte Carlo design studies of the GCT Telescope for the Cherenkov Telescope Array, in: Proceedings of 34th International Cosmic Ray Conference, 2015. arXiv:1508.06088v1 [astro-ph.IM]
[23] D. Dumas, et al., SST dual-mirror telescope for Cherenkov Telescope Array: an innovative mirror manufacturing process, in: Proceedings of SPIE, 9151, 91512U, 2014.
[24] P. Laporte, et al., Automatic performance budget: towards a risk reduction, in: Proceedings of SPIE, 9150, 91500X, 2014.